

47th AIAA Aerospace Science Meeting and Exhibit, Jan. 5-8, Orlando, Florida

Simulating turbulent viscous high-speed flows on unstructured grids

Suman Muppidi * & Krishnan Mahesh †
Aerospace Engineering & Mechanics
University of Minnesota

This paper discusses ongoing work on an all-Mach number, non-dissipative algorithm to solve compressible flows on unstructured grids. The algorithm is capable of handling unstructured grids, which allow efficient and speedy generation of computational meshes for complex geometries. The novel feature of the algorithm is an incompressible scaling for pressure that naturally yields the divergence-free condition for velocity as the Mach number goes to zero. The desirable feature of this algorithm is the discrete conservation of kinetic energy in the incompressible flow limit which in turn ensures robustness of the calculation at high Reynolds numbers without the need for any numerical dissipation. We employ a characteristic filter based shock capturing scheme that is applied as a predictor-corrector approach. As a result, shock capturing is active only in the regions of discontinuities, and provides accurate non-dissipative solutions away from the shocks. Results of the algorithm on representative validation flows are presented.

I. Introduction

Our objective is to develop algorithms for simulation of high speed compressible flows in complex geometries. High Reynolds numbers require algorithms that are robust without numerical dissipation. Since most flows at high speeds involve shocks, the algorithm needs to be capable of accurate resolution of shocks/discontinuities. Finally, unstructured computational grids make meshing engineering geometries viable, and the algorithm needs to be capable of handling these meshes. The basis of our scheme is a novel 'all-Mach number' algorithm for compressible flows proposed by Hou and Mahesh (2005). It discretely conserves kinetic energy in the limit of inviscid, incompressible flow, making it robust at high Reynolds numbers without any numerical dissipation. This algorithm was originally implemented on structured grids, and in this paper we discuss its extension to unstructured grids. Park and Mahesh (2007) describe a characteristic filter based shock capturing scheme that provides stable solutions in the presence of discontinuities. This paper also describes the implementation of this shock-capturing algorithm for the all-Mach number scheme.

This paper is organized as follows. Section II presents the salient aspects of the numerical scheme employed. Section III contains examples of flows solved using this algorithm, and section IV contains some concluding statements and lists ongoing and future work.

*Postdoctoral research associate, Aerospace Engineering & Mechanics

†Associate Professor, Aerospace Engineering & Mechanics, AIAA member

Copyright © 2009 by Suman Muppidi. Published by the American Institute of Aeronautics and Astronautics, Inc. with permission.

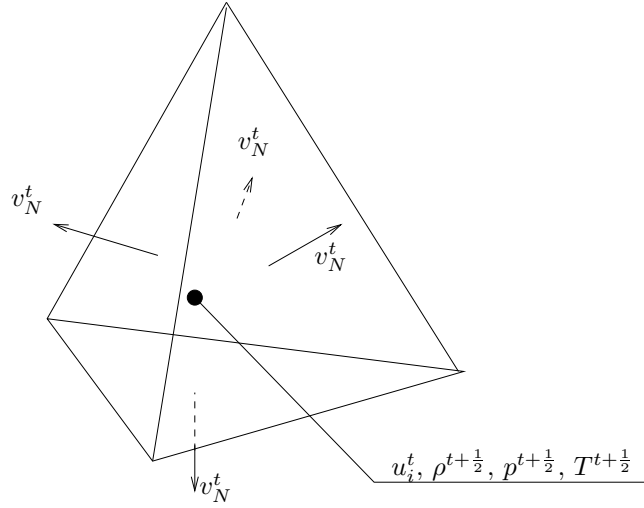


Figure 1. Schematic of a tetrahedral control volume showing the storage of variables. Face normal velocity v_N is defined at the face centroids, velocity u_i , pressure p , density ρ and temperature T are defined at the centroid of the control volume. Note that the variables are staggered in time.

II. Numerical scheme

A. Algorithm

The algorithm solves the compressible Navier–Stokes equations

$$\begin{aligned} \frac{\partial \rho^d}{\partial t^d} &= -\frac{\partial}{\partial x_k^d} (\rho^d u_k^d), \\ \frac{\partial \rho^d u_i^d}{\partial t^d} &= -\frac{\partial}{\partial x_k^d} (\rho^d u_i^d u_k^d + p^d \delta_{ik} - \sigma_{ik}), \text{ and} \\ \frac{\partial E_T^d}{\partial t^d} &= -\frac{\partial}{\partial x_k^d} \{ (E_T^d + p^d) u_k^d - \sigma_{ik} u_i^d - Q_k \}, \end{aligned} \quad (1)$$

where ρ^d , u_i^d , p^d and E_T^d are the dimensional density, velocity, pressure and total energy, respectively. The viscous stress σ_{ij} and heat flux Q_i are given by

$$\sigma_{ij} = \mu^d \left(\frac{\partial u_i^d}{\partial x_j^d} + \frac{\partial u_j^d}{\partial x_i^d} - \frac{2}{3} \frac{\partial u_k^d}{\partial x_k^d} \delta_{ij} \right), \text{ and} \quad (2)$$

$$Q_i = \frac{\mu^d C_p^d}{Pr} \frac{\partial T^d}{\partial x_i^d}, \quad (3)$$

where T^d is the dimensional temperature, and Pr is the Prandtl number. μ^d is the viscosity coefficient, and C_p is the specific heat at constant pressure. The novel feature of the algorithm proposed by Hou & Mahesh (2005) is the incompressible scaling for pressure. Density, velocity etc undergo standard non-dimensionalization, as follows.

$$\begin{aligned} \rho &= \frac{\rho^d}{\rho_r}, u_i = \frac{u_i^d}{u_r}, t = \frac{t^d}{L/u_r}, \\ p &= \frac{p^d - p_r}{\rho_r u_r^2}, Mr = \frac{u_r}{a_r}, T = \frac{t^d}{T_r} \end{aligned} \quad (4)$$

Mr is the reference Mach number, and a_r is the reference sound of speed. The following non-dimensional equations are obtained by rewriting equation 1 using equation 4.

$$\begin{aligned}
& \frac{\partial \rho}{\partial t} + \frac{\partial}{\partial x_j} (\rho u_j) = 0, \\
& \frac{\partial \rho u_i}{\partial t} + \frac{\partial}{\partial x_j} (\rho u_i u_j) = \frac{\partial p}{\partial x_i} + \frac{1}{Re} \frac{\partial \tau_{ij}}{\partial x_j}, \quad \text{and} \\
M_r^2 \left[\frac{\partial}{\partial t} \left(p + \frac{\gamma-1}{2} \rho u_i u_i \right) + \frac{\partial}{\partial x_j} \left(\gamma p + \frac{\gamma-1}{2} \rho u_i u_i \right) u_j \right] + \frac{\partial u_i}{\partial x_i} \\
= \frac{(\gamma-1) M_r^2}{Re} \frac{\partial \tau_{ij} u_i}{\partial x_j} + \frac{1}{Re Pr} \frac{\partial}{\partial x_j} \left(\frac{\mu \partial T}{\partial x_j} \right). \tag{5}
\end{aligned}$$

The non-dimensional equation of state is

$$\rho T = \gamma M_r^2 p + 1. \tag{6}$$

Note that this algorithm solves for pressure p (at every timestep) instead of the total energy E_T as is traditionally done while solving the compressible Navier Stokes equations. The second consequence of equation 5 is due to the factor M_r^2 that appears in the energy equation. As the reference Mach number goes to zero, the equations naturally yield

$$\frac{\partial u_i}{\partial x_i} = \frac{1}{Re Pr} \frac{\partial}{\partial x_i} \left(\frac{\mu \partial T}{\partial x_j} \right) \tag{7}$$

i.e. the velocity field is divergence free at constant temperature and density, a feature of incompressible Navier Stokes equations. It can be seen that when the spatial derivatives are written in a conservative form, the algorithm is discretely energy conserving in the low Mach number limit.

A finite volume approach is used to discretize the equations. Pressure, velocity and density are stored at the control volume centers, and the face-normal velocity is stored at the face centroids (figure 1). Note that the variables are staggered in time. The detailed discrete equations are described in Hou and Mahesh (2005) and will not be repeated here. One aspect to note is that the face normal velocity v_N is obtained by projection, and not interpolation. Also, the discretization is symmetric in time and space. Time-advancement of the solution is implicit, and the equations are solved using a predictor-corrector approach. At every time step, a pressure field is *predicted*. Density and momentum equations are advanced in time, and the latest density and momentum fields are used to *correct* the pressure. This iteration (at each time step) is continued until some convergence criteria is satisfied.

B. Extension to unstructured mesh

A finite volume approach is used to discretize the equations in 5. For example, the continuity equation can be written (by integrating the equation over the control volume, and by using Gauss's theorem to transform the volume integrals to surface integrals) as:

$$\frac{\partial}{\partial t} \rho_{cv} + \frac{1}{V} \sum_{faces} \rho_f v_N A_f = 0. \tag{8}$$

Here, ρ_{cv} is the cell centered density that is being advanced in time, V is the volume of the cell, ρ_f is the density at each face of the cell, v_N is the face normal velocity at each of the faces, and A_f is the face area. A schematic of a cell and the faces is shown in 2. Here the control volume (cell) $icv1$ has four faces, each of which contribute to the second term in equation 8. ρ_f is obtained by interpolation: $\rho_f = 0.5(\rho_{icv1} + \rho_{icv2})$. Discretizing the time derivative in equation 8 and evaluating the spatial derivative at $t + 1$ gives:

$$\frac{\rho_{cv}^{t+\frac{3}{2}} - \rho_{cv}^{t+\frac{1}{2}}}{\Delta t} + \frac{1}{V} \sum_{faces} \rho_f^{t+1} v_N^{t+1} A_f = 0. \tag{9}$$

ρ^{t+1} is further written as $0.5(\rho^{t+\frac{1}{2}} + \rho^{t+\frac{3}{2}})$, a symmetric interpolation in time. Note that that discretization along equation 9 does not require any information regarding the (Cartesian) orientation of the faces. The

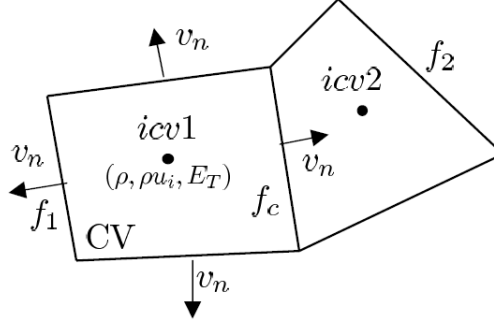


Figure 2. Schematic of the parallel faces on unstructured meshes, required for the shock capturing scheme. Computation of the filtered flux at face f_c requires information at faces f_1 and f_2 .

momentum equation is similarly discretized as

$$\frac{g_{i,cv}^{t+1} - g_{i,cv}^t}{\Delta t} + \frac{1}{V} \sum_{faces} g_{i,f}^{t+\frac{1}{2}} v_N^{t+\frac{1}{2}} A_f = -\frac{\partial}{\partial x_i} p_{cv}^{t+\frac{1}{2}} + \frac{1}{Re} \frac{1}{V} \sum_{faces} (\tau_{ij})_f^{t+\frac{1}{2}} N_j A_f. \quad (10)$$

Here, $g_i = \rho u_i$ denotes the i component of momentum, and τ_{ij} is the shear stress. N_j is the outward face normal of the face. $p_{cv}^{t+\frac{1}{2}}$ is written as

$$p_{cv}^{t+\frac{1}{2}} = \frac{1}{4} \left\{ p_{cv}^{t-\frac{1}{2}} + 2p_{cv}^{t+\frac{1}{2}} + p_{cv}^{t+\frac{3}{2}} \right\}, \text{ and} \\ v_N^{t+\frac{1}{2}} = \frac{1}{2} (v_N^t + v_N^{t+1}) \quad (11)$$

The discrete energy equation becomes:

$$M_r^2 \left\{ \frac{\partial}{\partial t} \left(p_{cv} + \frac{\gamma-1}{2} \rho u_i u_i \right)^{t+\frac{1}{2}} + \frac{1}{V} \sum_{faces} \left(\gamma p_{cv} + \frac{\gamma-1}{2} \rho u_i u_i \right)_f^{t+\frac{1}{2}} v_N^{t+\frac{1}{2}} A_f \right\} + \frac{1}{V} \sum_{faces} v_N^{t+\frac{1}{2}} A_f \\ = \frac{(\gamma-1)M_r^2}{Re} \frac{1}{V} \sum_{faces} (\tau_{ij} u_i)_f^{t+\frac{1}{2}} N_j A_f + \frac{1}{Re} \frac{1}{Pr} \frac{1}{V} \sum_{faces} \left(\mu \frac{\partial T^{t+\frac{1}{2}}}{\partial N} \right) A_f, \quad (12)$$

where $\frac{\partial}{\partial N}$ denotes the derivative across (normal to) the face. T is the temperature (obtained using the equation of state), and N_j is the face normal. As mentioned earlier, this system of discrete equations 9 – 12 is solved using a predictor–corrector approach.

C. Shock capturing

The algorithm uses a shock–capturing scheme that was originally proposed by Yee *et al.* (1999) for structured meshes and was extended by Park & Mahesh (2007) to unstructured meshes. Shock-capturing for non-dissipative schemes can be performed either by adding a filter, or hybridization with an upwind scheme. Here, the filtering technique is employed since the filter can be independently implemented with base scheme by predictor-corrector-like scheme. Once a physical time step Δt is advanced to get the solution $\hat{\mathbf{q}}^{n+1}$ from \mathbf{q}^n , the final solution \mathbf{q}^{n+1} at $t + \Delta t$ is determined from a corrector-like scheme:

$$\mathbf{q}_{cv}^{n+1} = \hat{\mathbf{q}}_{cv}^{n+1} - \frac{\Delta t}{V_{cv}} \sum_{faces} (\mathbf{F}_f^* \cdot \mathbf{n}_f) A_f, \quad (13)$$

where \mathbf{F}_f^* is the filter numerical flux. \mathbf{q}^n and \mathbf{q}^{n+1} are the conserved variable arrays at time step n and $n + 1$, and $\hat{\mathbf{q}}^{n+1}$ is the set of variables at time step $n + 1$ but prior to the application of shock–capturing.

Shock-capturing scheme is easily isolated from the base scheme and independent modification/refinement of each is possible. The original scheme (Yee *et al.*) requires information about variables at adjacent grid elements. Since this information is not always available on unstructured meshes, the scheme is modified so as to use the information at the parallel faces f_1 and f_2 to compute the filtered fluxes at the face f_c . A schematic of the control volume visualizing these faces is given in figure 2. Park & Mahesh define f_1 (f_2) as the most parallel face to f_c among all the faces f that surround $icv1$ ($icv2$) except for f_c itself ($\equiv \{f\}_{icv1(icv2)}$). Practically, $f_1 \in \{f\}_{icv1}$ and $f_2 \in \{f\}_{icv2}$ are planes such that

$$\varphi(f, f_c) = 1 - |\mathbf{n}_{f_c} \cdot \mathbf{n}_f|. \quad (14)$$

has the minimum possible value. The filter numerical flux has the form

$$\mathbf{F}_{f_c}^* = \frac{1}{2} \mathbf{R}_{f_c} \Phi_{f_c}^*, \quad (15)$$

where \mathbf{R} is the right Eigenvector of (convective flux vector) $= [\bar{\rho}_f v_N, (\bar{\rho} \tilde{u}_i)_f v_N + \bar{p}_f n_i, (\bar{E}_T + \bar{p})_f v_N]^T$ ($i = 1, 2, 3$). The face value $\mathbf{R}_{f_c} = \mathbf{R}(\mathbf{q}_{icv1}, \mathbf{q}_{icv2})$ is constructed using Roe's average:

$$\begin{aligned} \mathbf{u}_{f_c, \text{Roe}} &= \frac{\sqrt{\rho_{icv1}} \mathbf{u}_{icv1} + \sqrt{\rho_{icv2}} \mathbf{u}_{icv2}}{\sqrt{\rho_{icv1}} + \sqrt{\rho_{icv2}}}, \\ H_{f_c, \text{Roe}} &= \frac{\sqrt{\rho_{icv1}} H_{icv1} + \sqrt{\rho_{icv2}} H_{icv2}}{\sqrt{\rho_{icv1}} + \sqrt{\rho_{icv2}}}, \\ c_{f_c, \text{Roe}}^2 &= (\gamma - 1) \left[H_{\text{roe}} - \frac{1}{2} (u_{f_c, \text{Roe}}^2 + v_{f_c, \text{Roe}}^2 + w_{f_c, \text{Roe}}^2) \right], \end{aligned} \quad (16)$$

where $H = (E_t + p) / \rho$ is the enthalpy and c is the speed of sound. On the other hand, the expression for the ℓ -th component of Φ^* , $\phi^{*\ell}$ is given by

$$\phi_{f_c}^{*\ell} = \kappa \theta_{f_c}^\ell \phi_{f_c}^\ell, \quad (17)$$

where κ is the adjustable parameter and θ_{f_c} is the switch function given by

$$\begin{aligned} \theta_{f_c} &= \sqrt{0.5 \left(\hat{\theta}_{icv1}^2 + \hat{\theta}_{icv2}^2 \right)}, \\ \hat{\theta}_{icv1} &= \left| \frac{|\alpha_{f_c}| - |\alpha_{f_1}|}{|\alpha_{f_c}| + |\alpha_{f_1}|} \right|^p, \\ \hat{\theta}_{icv2} &= \left| \frac{|\alpha_{f_2}| - |\alpha_{f_c}|}{|\alpha_{f_2}| + |\alpha_{f_c}|} \right|^p. \end{aligned} \quad (18)$$

Here, $\alpha_f = \mathbf{R}_f^{-1} \Delta \mathbf{q} = \mathbf{R}_f^{-1} (\mathbf{q}_{icv2} - \mathbf{q}_{icv1})$ is the difference of the characteristic variable across the face, and $p = 1$ is used. Note that the formulation θ_{f_c} in Eq. (18) is a code-friendly variation of the original formulation of Yee *et al.* $\theta_{f_c} = \max(\hat{\theta}_{icv1}, \hat{\theta}_{icv2})$ for the case $icv1$ and $icv2$ belong different processors in MPI-based parallel algorithm, and is proven to make a negligible difference with the original formulation. For ϕ^ℓ , the Harten-Yee TVD is chosen: form

$$\phi_{f_c}^\ell = \frac{1}{2} \Psi(a_{f_c}^\ell) (g_{icv1}^\ell + g_{icv2}^\ell) - \Psi(a_{f_c}^\ell + \gamma_{f_c}^\ell) \alpha_{f_c}^\ell, \quad (19)$$

$$\gamma_{f_c}^\ell = \frac{1}{2} \frac{\Psi(a_{f_c}^\ell) (g_{icv2}^\ell - g_{icv1}^\ell) \alpha_{f_c}^\ell}{(\alpha_{f_c}^\ell)^2 + \epsilon}, \quad (20)$$

where $\epsilon = 10^{-7}$ and $\Psi(z) = \sqrt{\delta + z^2}$ ($\delta = 1/16$) is introduced for the entropy fixing. $a_{f_c}^\ell$ is the element of the eigenvalues. According to Yee *et al.*, g_{icv}^ℓ 's are cell center values defined in terms of α_f^ℓ 's. One possible expression in the structured mesh is

$$g_{i,j,k}^\ell = \text{minmod} \left(\alpha_{i,j-1/2,k}^\ell, \alpha_{i,j+1/2,k}^\ell \right) \quad (21)$$

along j -direction. Yee *et al.* provide other types of limiters. Note that these limiters depend on the orientation of the faces. Such a definition is not the most applicable when dealing with unstructured meshes where the concept of Cartesian directions does not exist. Park & Mahesh overcome this by defining g 's at cell faces to account for this directional dependence. Noting that the required quantities are the symmetric average and difference, $(\frac{1}{2}(g_{icv1} + g_{icv2}))$ and $(\frac{1}{2}(g_{icv2} - g_{icv1}))$, they suggest the definition of these quantities at cell faces:

$$g_{f_c}^{+\ell} \equiv \frac{1}{2} \{ \text{minmod}(\alpha_{f_1}^\ell, \alpha_{f_c}^\ell) + \text{minmod}(\alpha_{f_c}^\ell, \alpha_{f_2}^\ell) \}, \quad (22)$$

$$g_{f_c}^{-\ell} \equiv \frac{1}{2} \{ \text{minmod}(\alpha_{f_2}^\ell, \alpha_{f_c}^\ell) - \text{minmod}(\alpha_{f_1}^\ell, \alpha_{f_c}^\ell) \}. \quad (23)$$

Accordingly, $\phi_{f_c}^\ell$ and $\gamma_{f_c}^\ell$ are rewritten as follows:

$$\phi_{f_c}^\ell = \Psi(a_{f_c}^\ell) g_{f_c}^{+\ell} - \Psi(a_{f_c}^\ell + \gamma_{f_c}^\ell) \alpha_{f_c}^\ell, \quad (24)$$

$$\gamma_{f_c}^\ell = \frac{\Psi(a_{f_c}^\ell) g_{f_c}^{-\ell} \alpha_{f_c}^\ell}{(\alpha_{f_c}^\ell)^2 + \epsilon}, \quad (25)$$

Note that the extension of the scheme to unstructured meshes is done in a self-consistent manner. Since no interpolation is required between cell center and face values, this approach can guarantee the same result as what could be obtained from the original formulation, when a structured grid is used. The filter proposed by Yee *et al.* was found to be dissipative when applied to an isotropic turbulence problem (Park & Mahesh). To further localize the dissipation, the Harten-Yee filter is modified with the idea of Ducros *et al.* (1999) by multiplying the following sensor to θ_{f_c} in equation 18:

$$\theta_{f_c}^* = \frac{1}{2} (\theta_{icv1}^* + \theta_{icv2}^*), \quad (26)$$

$$\theta_{icv1}^* = \frac{(\nabla \cdot \mathbf{u})_{icv1}^2}{(\nabla \cdot \mathbf{u})_{icv1}^2 + \Omega_{icv1}^2 + \epsilon}, \quad (27)$$

where Ω is the vorticity magnitude and $\epsilon = 10^{-7}$ is a small positive value.

Note that the underlying algorithm solves for pressure, and the shock capturing technique requires the application of filtered fluxes on the total energy E_T . At every time step, hence, \hat{E}_T is computed using $\hat{\rho}$, \hat{u}_i and \hat{p} . The filtered fluxes are applied, and the corrected values are computed for ρ , u_i and E_T – which are used to compute the pressure p . Also note that the conserved variables are stored staggered in time: u_i at t , $t + 1$ etc, and ρ , p at $t + \frac{1}{2}$, $t + \frac{3}{2}$ etc. The computation of the filtered fluxes needs all the required variables to be at the same time level. Shock capturing is applied in a consistent manner after interpolating pressure and density to time $t + 1$.

III. Results

A. Flow past blunt bodies

1. Cylinder

A canonical test problem for high speed external flows is the supersonic flow past a cylinder, results of which are shown in figure 3. In this case, the flow is from the left to the right, and corresponds to the conditions of simulations by Zhong (1997). The Mach number is 5.73, and the Reynolds number is 2050. The mesh used for the simulation consists of 192 elements (hexahedral) in both wall normal and the azimuthal directions. Figure 3 shows contours of density, velocity component v , divergence and pressure. The detached shock upstream of the cylinder is visible. The results of interest in this problem are the variation (jump) of the conserved variables across the shock, and that along the surface of the cylinder. Figure 4(a) shows the variation of pressure along the body of the cylinder as a function of the azimuthal angle θ . Note that the results compare well with existing results. Figure 4(b) shows the variation of pressure, streamwise velocity u and density along the symmetry line ($y = 0$).

A grid convergence study for this problem was performed using a (coarse) grid that contained 80 elements in the azimuthal direction and 60 in the normal direction. Figure 5 compares the C_p vs θ curves obtained

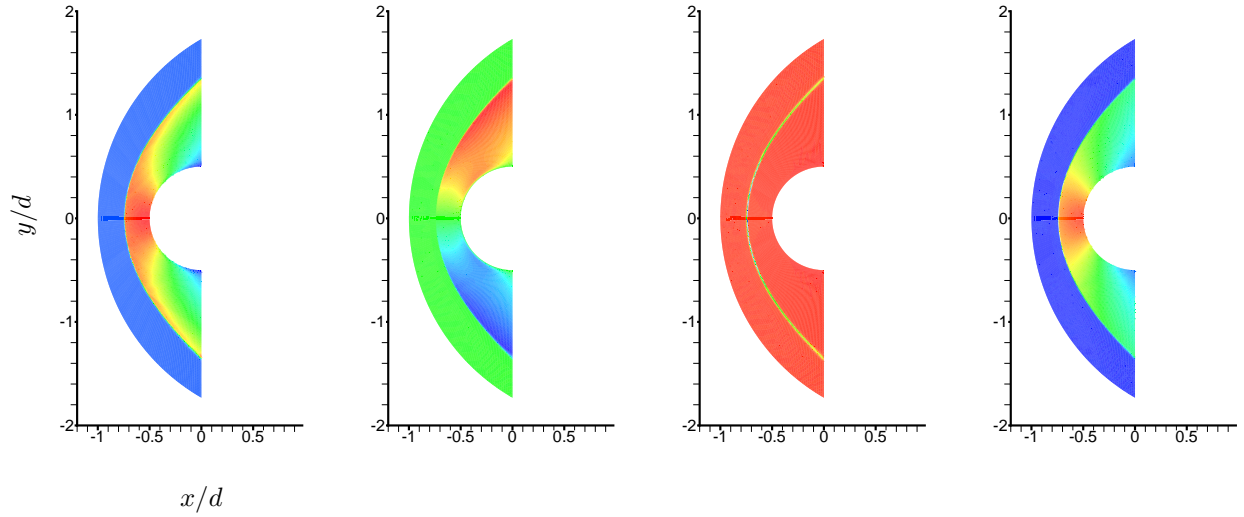


Figure 3. Flow past a half cylinder at Mach 5.73. Adiabatic boundary conditions for temperature are applied at the wall of the cylinder. Pictures show contours of density, velocity v , divergence and pressure.

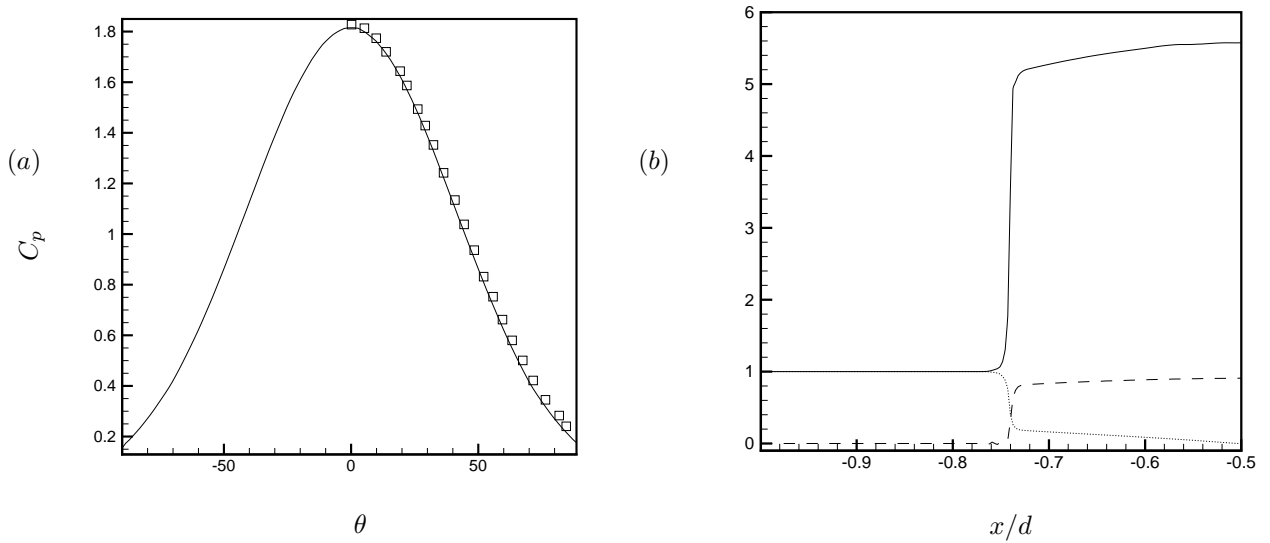


Figure 4. (a) Comparison of pressure along the surface of the cylinder. — simulation. \square Zhong (1997). (b) Variation of density (—), C_p (----) and streamwise velocity u (.....) along the symmetry line.

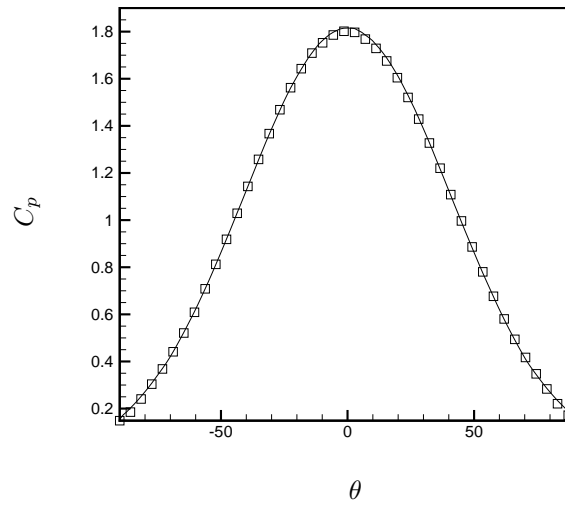


Figure 5. Grid convergence for the flow past cylinder. Figure shows variation of C_p with θ using two computational grids. 192×192 (—) and 80×60 (\square). The agreement appears to be reasonable.

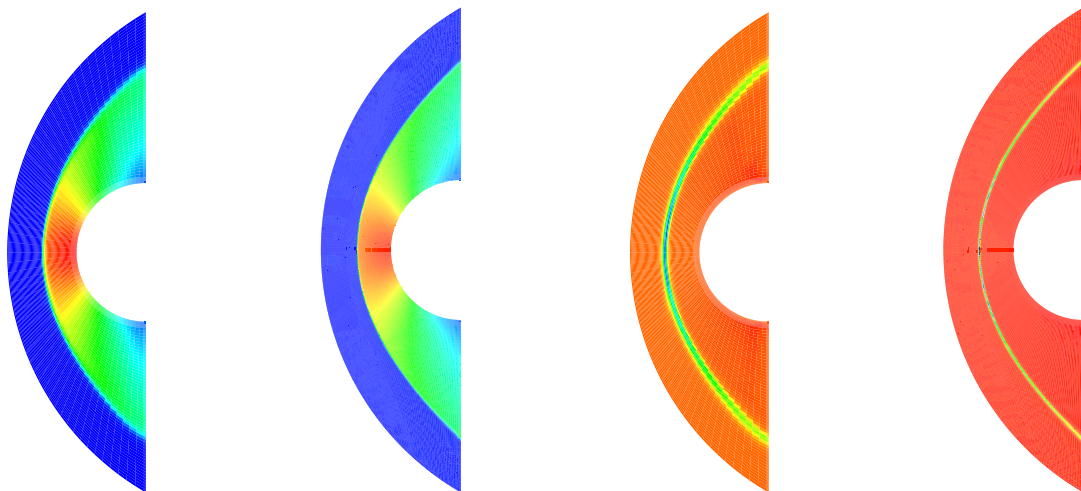


Figure 6. Grid convergence for the flow past cylinder. Contours of pressure and divergence. The shock is visibly sharper/thinner on the fine mesh.

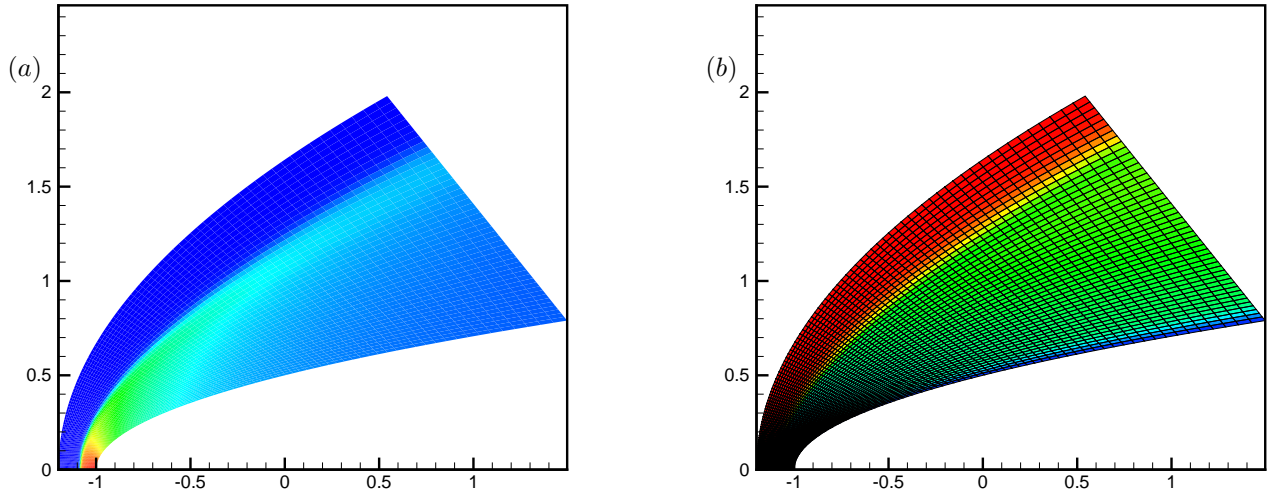


Figure 7. Contours of (a) pressure and (b) Mach number for flow past a parabolic blunt body. The Mach number is 5, and Reynolds number is 5025.

using the two different grids. Even the coarse mesh calculation predicts the pressure at the wall reasonably well. Figure 6 compares the contours of pressure and divergence using the two grids. The biggest difference, as must be expected, is shown by the contours of divergence. The shock is thicker on the coarse mesh.

2. Parabolic blunt body

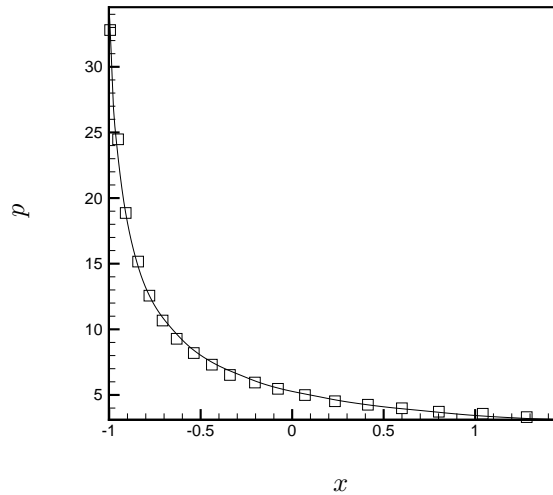


Figure 8. Variation of pressure along the surface. — simulation. □ Zhong (1997).

The solver was used to simulate the flow past a parabolic blunt body, as shown in figure 7. The flow is from left to the right, the Mach number is 5, and the Reynolds number is 5025. The parabolic surface is given by $x = by^2 - d$ and the nose radius of curvature is $r = 1/(2b)$. $b=4$ and $d=1$ are constants. The mesh used for these preliminary simulations flow consists of 48 points in the wall normal direction and 64 points in the wall parallel direction. No-slip velocity and adiabatic temperature boundary conditions are applied at the wall, and steady freestream conditions are applied at the inflow. Figure 7(a) shows the contours of

pressure. The detached shock is clearly visible. The shock is strongest near the symmetry line($y = 0$) and grows weaker away from it. Figure 7(b) shows the contours of Mach number, along with the computational mesh. Note that the mesh near the shock is neither very fine, nor particularly aligned with the shock. Yet, the resolution across the shock appears to be acceptable. Figure 8 shows the variation of pressure along the surface of the parabolic blunt body. The peak pressure occurs on the stagnation point ($y = 0.0$) and decreases thereafter. The figure also shows the profile of Zhong (1997), and the agreement appears to be reasonable.

B. Unsteady shock-vortex interaction

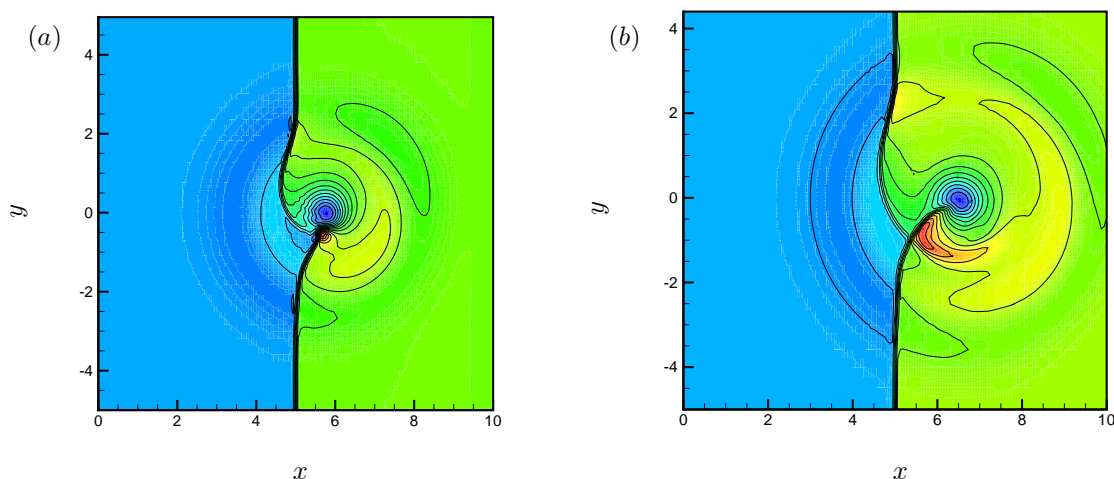


Figure 9. Convection of vortex through a shock (Mach 1.2). Contours of pressure. Figures show solution at two different instances in time as the vortex convects from the left to the right.

Figure 9 shows the evolution of a solution where a vortex convects through a shock. The vortex is initialized as

$$\begin{aligned}
 u &= 1 - \frac{C(y - y_c)}{R^2} \exp(-r^2/2), \\
 v &= \frac{C(x - x_c)}{R^2} \exp(-r^2/2), \\
 p &= p_\infty - \frac{\rho C^2}{2R^2} \exp(-r^2),
 \end{aligned} \tag{28}$$

where $r^2 = ((x - x_c)^2 + (y - y_c)^2)/R^2$. Here, $R = 1$, $C = 0.8$. At $t=0$, the normal shock is at $x = 5$, and the vortex is centered at $x=x_c = 3.0$. The vortex is convected from left to right at a convection speed of unity. The Mach number is 1.2. Figures 9(a) and (b) show the solution at time of 3 and 4 units respectively. The deformation of both the shock and the vortex, due to their mutual interaction is clearly seen. As the vortex leaves the domain, the normal shock regains its shape.

C. Shock boundary layer interaction

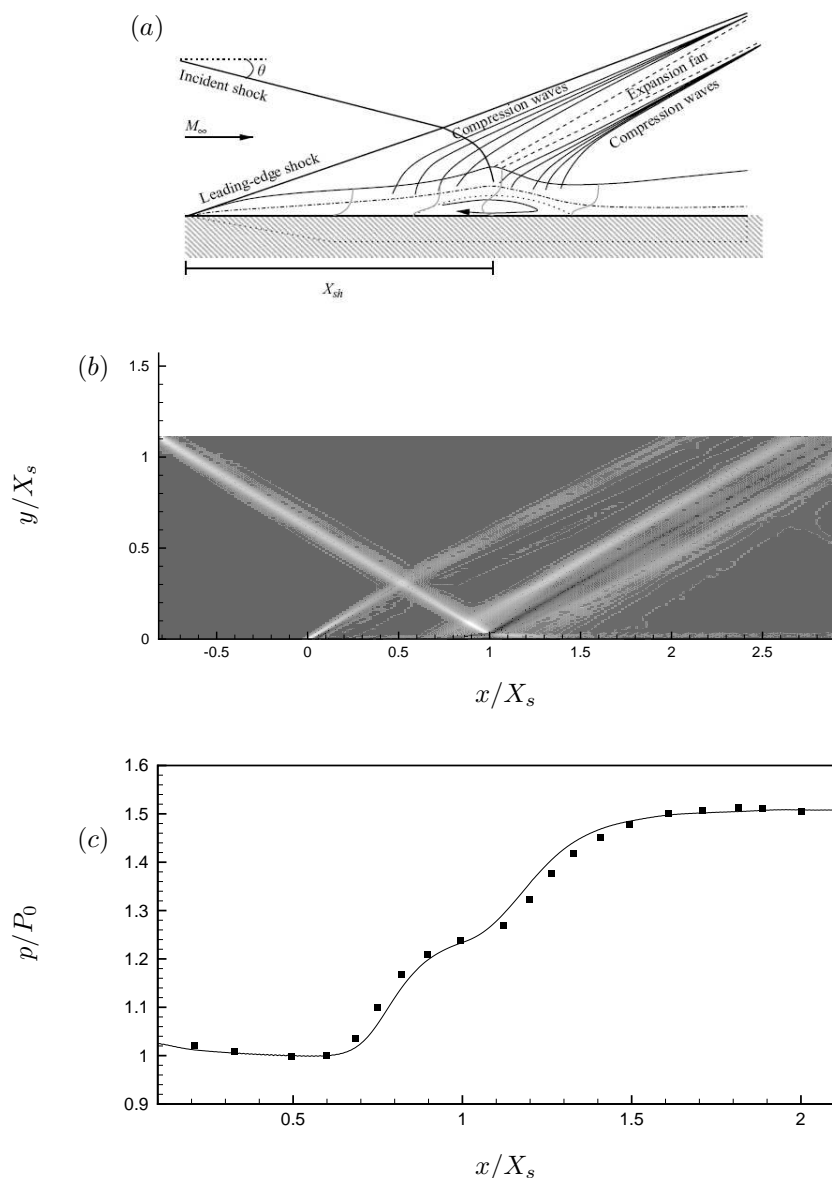


Figure 10. Interaction of an incident shock with a laminar boundary layer. (a) shows a schematic of the problem (reproduced from Robinet 2007) (b) shows a numerical Schlieren, and (c) shows wall pressure variation (lines - present simulation, symbols - experimental results of Degrez *et al.* 1987.)

Shock wave boundary layer interactions occur in many high speed flows, and can significantly alter both aerodynamic and thermal loads. The interaction between the compressible effects (dependent mainly on the Mach number) and the viscous effects (a function of the Reynolds number) makes the problem challenging. Figure 10(a) shows the schematic of the interaction between a boundary layer, and a shock incident upon it. The flow is characterized by detachment of the boundary layer, a separation region, and reattachment. Comprehensive reviews of the flowfield, the predictive and computational capabilities, and issues are presented in Delery & Panaras (1996), Knight & Degrez (1998), and Dolling (2000).

Figures 10(b) and (c) show results of a two-dimensional simulation at conditions corresponding to Degrez *et al.* (1987). The Mach number of the incoming flow is 2.15 and the angle of shock incidence is $\theta = 30.8^\circ$. The Reynolds number is 10^5 . Figure 10(b) is a numerical Schlieren and indicates the incident and the reflected shocks, and the separation region. Note the leading edge shock produced by the boundary layer. The axes are non-dimensionalized using X_s , the distance to the shock-impingement location from the origin of the

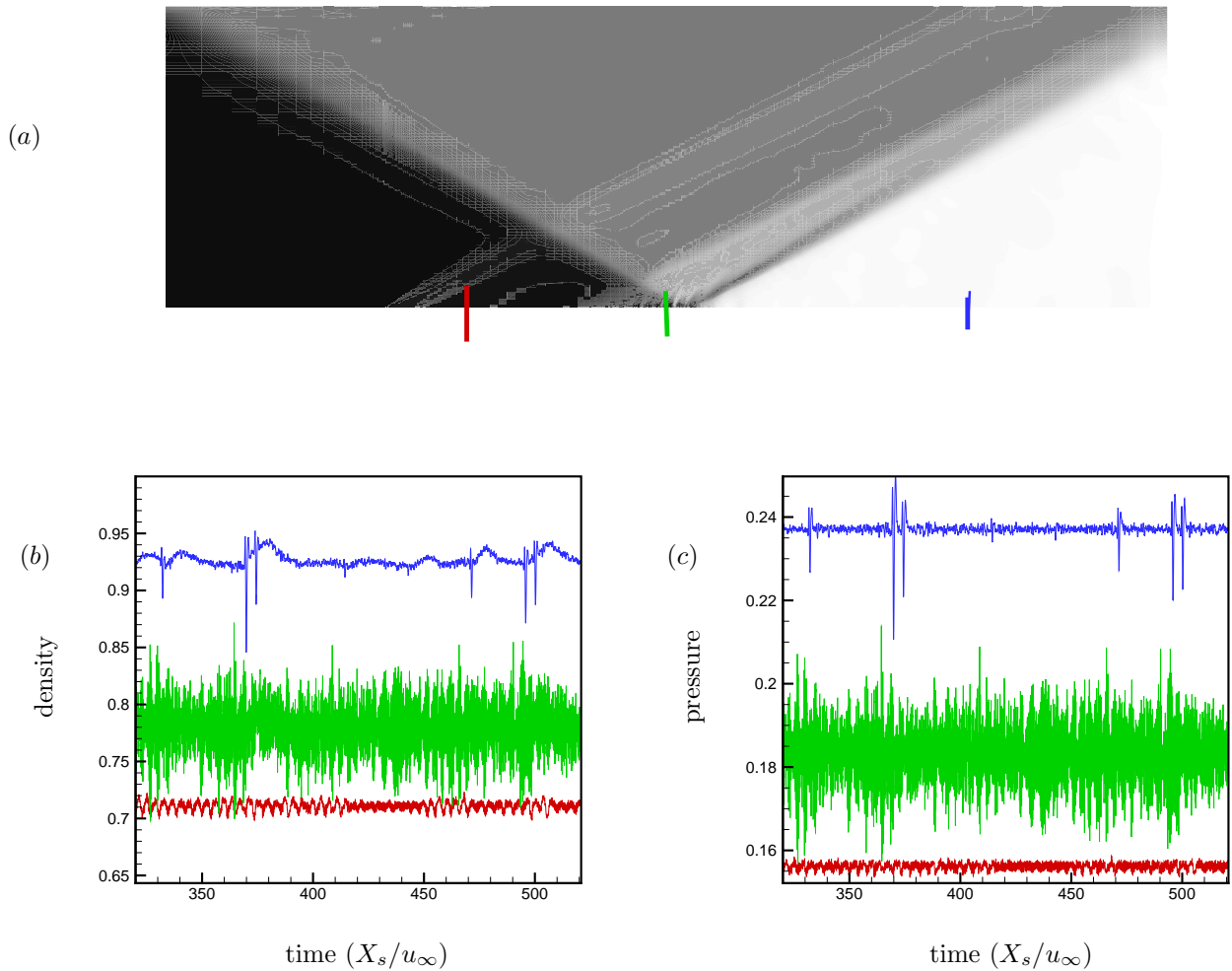


Figure 11. (a) Contours of pressure when the Reynolds number is ten times that in figure 10. At this Re , the shock boundary layer interaction is unsteady, as can be seen from the time history of (b) density, and (c) pressure. The three curves correspond to three different locations along the wall, as indicated in (a).

boundary layer. Figure 10(c) compares the horizontal variation of the wall pressure from the simulation with that of the experiment. Reasonable agreement is obtained. At these conditions, the flow is found to be steady. However, as the Reynolds number is increased by a factor of ten, the flow is observed to be unsteady. Figure 11(a) shows a snapshot of the flow at this higher Reynolds number, and the unsteadiness in the interaction region is visible. The unsteadiness begins at the shock impingement location and travels both downstream and upstream (up to the origin of the boundary layer). The extent of the unsteadiness can be observed from figures 11(b) and (c) which show the time history of density and pressure at three locations along the wall. The location of these points, in relation to the flow domain is indicated in figure 11(a).

IV. Conclusions and future work

A novel non-dissipative all-Mach number algorithm for compressible flows (Hou & Mahesh 2005) has been extended for unstructured meshes. It employs a characteristic filter based shock capturing technique (Park & Mahesh 2007) and is capable of solving high-Mach number flows. Some results for supersonic flow past blunt bodies are presented, where the algorithm shows good agreement with existing results. Future work will involve the use of this algorithm to study transition in high speed boundary layers, and simulation of supersonic flow past a conical blunt body.

Acknowledgments

This work is supported by the Air Force Office of Scientific Research under contract FA9550-04-1-0341 and by NASA under the hypersonics NRA program. We are grateful to Dr Noma Park for many useful discussions.

References

- ¹G. Degrez, C. H. Boccadoro & J. F. Wendt, 1987 The interaction of an oblique shock wave with a laminar boundary layer revisited. An experimental and numerical study *J. Fluid. Mech* **177**: 247–263 .
- ²J. M. Delery & A. G. Panaras, 1996 Shock-Wave/Boundary-Layer Interactions in High-Mach-Number Flows *AGARD AR-319*.
- ³D. S. Dolling, 2001 Fifty Years of Shock-Wave/Boundary-Layer Interaction Research: What Next? *AIAA J.* **39**:1517–1531.
- ⁴F. Ducros, V. Ferrand, F. Nicoud, C. Weber, D. Darracq, C. Gacherieu and T. Poinso, 1999, Large-eddy simulation of the shock/turbulence interaction, *J. Comput. Phys.* **152**: 517–549.
- ⁵Y. Hou and K. Mahesh, 2005, A robust colocated implicit algorithm for direct numerical simulation of compressible turbulent flows, *J. Comput. Phys.* **205**:205–221.
- ⁶D. D. Knight & G. Degrez, 1998 Shock Wave Boundary Layer Interactions in High Mach Number Flows. A Critical Survey of Current Numerical Prediction Capabilities. *AGARD AR-319*.
- ⁷N. Park and K. Mahesh 2007, Numerical and Modeling issues in LES of compressible turbulence on unstructured grids, *AIAA Paper 2007-0722*:1–18.
- ⁸A. Rohde, 2001, Eigenvalues and Eigenvectors of the Euler equations in general geometries, *AIAA paper 2001-2609*:1–6.
- ⁹H. C. Yee, N. D. Sandham, and M. J. Djomehri, 1999, Low-dissipative high-order shock-capturing methods using characteristic-based filters, *J. Comp. Phys.* **150**: 199–238.
- ¹⁰X. Zhong, 1997 Direct numerical simulation of hypersonic boundary-layer transition over blunt leading edges. I - A new numerical method and validation. *AIAA Paper 1997-0755*:1–26.